Systematic Methodology for an Optimized Design of Shape Memory Alloy-Driven Continuum Robots

Yannik Goergen,* Gianluca Rizzello, and Paul Motzki

Continuum robots stand out due to their high dexterity, which allows them to effectively navigate in confined spaces and dynamic environments. At present, motor-controlled tendons represent the most prominent actuation method used in continuum robots which require large drive units, increasing the overall system size and weight. A potential alternative technology to overcome those limitations is represented by shape memory alloy (SMA) wire actuators, which are characterized by extremely high energy density and flexibility, leading to a reduction of the size, weight, and design complexity of continuum robots. The complex thermomechanical behavior of SMA wires, however, makes the design of SMA-based applications a challenging task, and systematic approaches to design SMA-driven continuum robots are poorly understood. To overcome this issue, this article presents a novel systematic methodology for designing SMA-driven continuum robots capable of motion in a three-dimensional environment. First, the kinematic relationship between SMA wires and continuum robot deformation as well as the required actuator force in quasi-static conditions, is mathematically described based on the assumption of a constant curvature deformation. Subsequently, the model is validated by in-plane experiments for different design parameters. Based on the results, a fully integrated, antagonistic SMA continuum robot is built and validated.

1. Introduction

Inspired by continuously bending structures like the mammalian tongue or an elephant's trunk, continuum robots have gained increased interest in research over the past years. Unlike
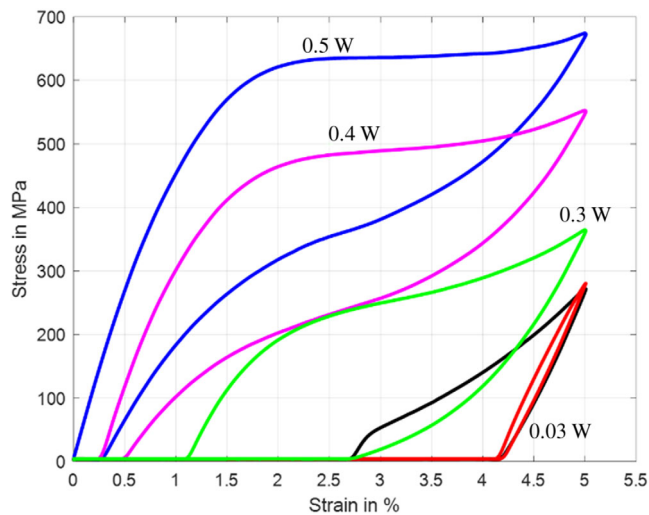
Y. Goergen, G. Rizzello, P. Motzki
Intelligent Materials Systems Lab
Department of Systems Engineering
Department of Materials Science and Engineering
Saarland University
66123 Saarbrücken, Germany
E-mail: yannik.goergen@imsl.uni-saarland.de

Y. Goergen, P. Motzki
Intelligent Materials Systems Lab
Center for Mechatronics and Automation Technology
ZeMA gGmbH
66121 Saarbrücken, Germany

The ORCID identification number(s) for the author(s) of this article can be found under https://doi.org/10.1002/adem.202301502

conventional robots, which achieve high position accuracy and repeatability in well-defined environments by means of rigid links and joints,[1,2] continuum robots are able to follow complex paths and adapt to unstructured environments thanks to their hyperflexible structure, which lacks rigid links and joints. Combining the improved dexterity and flexibility of continuum robots with a soft structure allows to increase safety during interactions with humans, thus opening up, ranging from medicine[3] and minimally invasive surgery[4–8] to nuclear reactor maintenance,[4] exploration,[5] navigation[6] as well as endoscopy.[7] Generally, continuum robots can be categorized in terms of their structure and actuation strategy. Common structural designs include concentric-tube robots, based on multiple precurved elastic tubes nested inside each other,[8,9] as well as single backbone continuum robots, in which an elastic element structure supports the structure and acts as a restoring force, which brings back the robot to its initial state after actuation.[7,10,11] The actuation strategy can be categorized as intrinsic or extrinsic, depending on where the actuation takes place with respect to the structure. Intrinsic actuation refers to actuation within the bending structure, while the extrinsic actuation method takes place outside the moving robot and requires suitable mechanisms to transmit the force to the structure.[12] Tendon-driven actuation represents the most common type of extrinsic technology,[13,14] while commonly used intrinsic actuators include pneumatics,[15] hydraulics as well as smart materials like for example shape memory alloys (SMA) or electroactive elastomers.[16] Tendon-driven mechanisms, as well as pneumatics and hydraulics, can generate a large displacement and thus achieve a high bending angle of the continuum robot within a comparably small installation space. In contrast, these actuator mechanisms require large drive units, which in turn limit the miniaturization and portability of the overall system.[17–20]

In contrast, SMA wire actuators allow full integration into the continuum robotic structure. SMA wires exhibit a macroscopic elongation (on the order of 6%) when subject to mechanical stress, and contract to their original state when heated up. This reversible process represents the basic principle that allows using SMA wires as contractile actuators.[21] Controlling the length of an SMA wire is achieved by actively heating it, e.g., via an electric current.[22] Based on the in situ actuation, SMA

Figure 1. Stress–strain characteristics for different constant power values (left).

wire actuators offer a means to improve the miniaturization of the overall system. Besides, SMAs feature the highest energy density among known actuator technologies (on the order of $10^7 \, \text{J m}^{-3}$[23]), which allows to develop highly compact and light-weight systems.[24–26] Despite their advantages, the mechanical stress–strain characteristic of SMA is highly hysteretic and temperature-dependent[22,27–30] (see **Figure 1**), making the design, modeling, and control of SMA systems highly challenging.

This highly nonlinear response also poses challenges when developing complex SMA-driven systems such as continuum robots. Compared to tendon-driven actuation, the limited reversible strain of shape memory alloys (which also affects the material lifetime[31–33]) requires suitable design solutions to convert it into a maximum continuum robot's performance, e.g., maximum bending angle. Moreover, the strongly nonlinear and temperature-dependent elastic response of SMAs may significantly compromise the robot bending performance, if not properly accounted for during the system design (e.g., the SMA may not be strong enough to dominate the elastic restoring force of the backbone element and/or other involved forces). To meet the performance requirements of target continuum robotic systems, e.g., bending displacement, the limited SMA strain as well as the SMA wire stiffness need to be explicitly accounted for during the design phase. This process becomes especially important for 3D-bending continuum robots, in which the kinematic and elastic response of multiple SMA wires working against each other need to be explicitly accounted for. Compared to tendon-driven continuum robots, not a lot of research has been published on the systematic design of SMA-driven continuum robots.

Table 1 shows an overview of relevant research work regarding SMA-driven continuum robotic structures. Except for ref. [34], the research mainly focuses on different mechanical designs for various applications, such as endoscopy or colonoscopy as well as an explanatory experimental validation. Additionally, different kinematic models as well as control strategies for continuum robots have been developed.[35,36] However, the mechanical design optimization as well as the combination of a general

kinematic model in combination with SMA actuator wires have not been addressed yet. In ref. [34], an optimization of an SMA-driven catheter is presented, targeting a minimum radius of curvature. This article explicitly focuses on the optimization of the catheter radius of curvature, whereas the presented work gives a general model which allows the optimization of any target performance requirement of an SMA-driven continuum robot. In addition, a quasi-static design method is presented, simplifying the design process presented in ref. [34], which is based on complex model-based design optimization algorithms. Previous work from the authors mainly focused on the mechanical design of SMA-driven continuum robots for different applications, the unique assembly procedure required to determine the suitable prestrain of the SMA wires while assembling as well as exemplary validation experiments.[7,11,37] The calculations presented in these publications are based on a highly simplified kinematic model neither incorporating the SMA characteristics nor accounting for multiple SMA actuators affecting each other.

In this article, a systematic design approach for SMA-driven continuum robots is presented. The structure integrates partially constrained SMA actuators by using equidistant distributed spacer disks along the elastic backbone,[11] see **Figure 2**. To design a robot with a target bending angle, kinematic, and quasi-static models are developed, which describe the dependency between SMA characteristics and kinematics of a continuum robot as well as the interaction among SMA forces and structural elasticity. Based on this model, a design procedure is explained, which provides a design guide to optimize an SMA-driven continuum robot for certain target specifications, e.g., maximum bending angle, followed by the description of the experimental setup. The performance of the developed robot is then experimentally evaluated and compared with the theoretical model predictions, confirming the validity of the presented approach. The obtained results show an agreement between measured bending angle and numerical prediction on the order of <5%, proving that the proposed quasi-static design method allows for an effective model-based design of SMA continuum robot without the need to use neither advanced finite element simulation tools nor complex model-based design optimization algorithms. The presented approach represents then a viable and systematic means to accelerate and simplify the design of continuum robots driven by SMA wire actuators. Thus, the presented work complements current research which is mainly focusing on the modeling and control optimization by providing a systematic methodology for optimizing mechanical design.

The remainder of this article is organized as follows: In Section 2, a general kinematic model of a tendon-driven continuum robot is presented and then extended by the SMA behavior. The model-optimized experimental prototype is then presented in Section 3, alongside the experimental validation of the model. Finally, the conclusion and outlook are discussed in Section 4.

2. Theoretical Modeling of SMA-Driven Continuum Robots

When designing an SMA continuum robot, there is a list of requirements that the system needs to meet. For example, in

Table 1. Overview of relevant research regarding SMA-driven continuum robots describing the publication focus as well as the limitations compared to this article.

Reference	Description	Focus	Limitations
[43], 2017	A soft actuator module consisting of four segments allowing for spatial motion using three SMA springs per segment is presented.	Mechanical design, self-sensing-based control, experimental validation.	No design optimizations, no model.
[44], 2017	A continuum robot of two segments enabling spatial motion using four SMA springs per segment is presented.	Mechanical design, kinematic model, experimental validation.	No design optimizations. Model does neither address design optimizations nor SMA-related limitations.
[34], 2012	A design optimization for a single-segment SMA-driven catheter is presented. The prototype consists of two opposing SMA actuator wires allowing for in-plane bending.	System model including an SMA constitutive model and kinematic relations, experimental validation.	Requires complex model-based design optimization algorithms. The model only accounts for optimizations regarding the radius of curvature.
[42,45], 2012	An octopus-inspired SMA-driven soft robot is presented. SMA springs are used as actuators to allow for spatial motion, stiffening, and elongating of the octopus arm.	Reproducing the octopus muscular hydrostat mechanism, design, and experimental validation.	No model
[36], 2023	A single-segment continuum robot driven by three springs is presented. The kinematic model as well as the control strategy are experimentally validated.	Kinematic model. Controller design for position control. Exemplary experimental validation.	No design optimizations. The model does neither address design optimizations nor SMA-related limitations.
[7], 2022	A single-segment continuum robot allowing for spatial motion using three SMA wires is presented and experimentally validated.	Mechanical design and fabrication, experimental validation.	No kinematic design optimizations. The model does neither address design optimizations nor SMA-related limitations.
[37], 2020	A modular design approach for multimodule SMA-driven continuum robots is presented including the assembly and fabrication of a single segment allowing for spatial motion using three SMA wires.	Modular system design, assembly process.	No model, no design optimizations.
[11], 2019	Prototypes for different applications are presented, all consisting of a single segment allowing for spatial motion using three SMA wires.	Basic kinematic model, assembly process, experimental validation.	No design optimizations. The model does neither address design optimizations nor SMA-related limitations.
[46], 2019	The design, fabrication, and experimental validation of a three-segment SMA-based continuum robot is presented. The spatial motion is realized by using three SMA springs per segment.	Mechanical design and fabrication, experimental validation.	No model, no design optimizations.
[47], 1988	The article describes a self-sensing-based control system of an SMA-driven continuum robot. A prototype consisting of five segments and actuated by SMA springs is built to validate the control strategy.	Mechanical design, control system design, experimental validation.	No model, no design optimizations.
[48], 2001	The article presents a new fabrication process of SMA sheets. A single-segment catheter actuated by three SMA sheets is presented and experimentally validated.	Mechanical design and fabrication, experimental validation.	No model, no design optimizations.
[49], 2006	Three segments. Spatial motion using three SMA springs per segment	Mechanical design, experimental validation	No model, no design optimizations.

the case of a robot envisioned for navigation or endoscopic applications, those may include the workspace of the Tool-Center-Point as well as the required actuator force to achieve the maximum bending (which depends on the stiffness of the continuum robotic structure). The model outlined within this section explains the interdependencies of the individual parameters, thus providing a theoretical design framework for SMA-based continuum robots.

Planar bending of a continuum robot, with partially constrained SMA actuators using equidistant distributed spacer disks, is considered in this work. A superelastic nickel-titanium (NiTi) rod is used as a restoring element.

The model provides a systematic design guide for SMA-driven continuum robots to meet specific performance criteria. Free design parameters are the diameter of the core element, the diameter and the prestrain of the SMA wire, as well as the continuum robot structure-related parameters, where the model derives all parameters based on any combination of two of the following parameters: the distance between SMA wire and core element, the robot backbone length, the maximum bending angle, and the corresponding curvature radius, see **Figure 3**. Furthermore, the number of required spacer disks is given by the model.

The model presented is based on the following assumptions: 1)The robot bends following a constant curvature kinematics[35]

**ADVANCED
SCIENCE NEWS**

www.advancedsciencenews.com

**ADVANCED
ENGINEERING
MATERIALS**

www.aem-journal.com

Figure 2. Prototypes of spatially bending SMA-driven continuum robots in different sizes (right) and the prototype being used in this article for validation experiments (left).
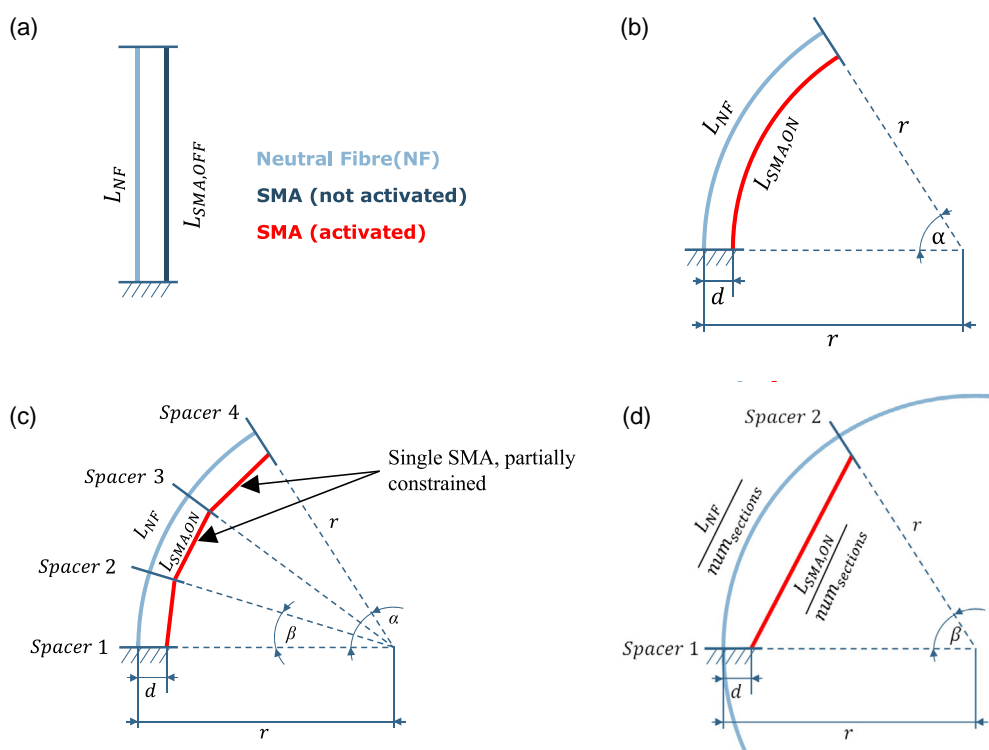
Figure 3. Schematic drawing of a continuum robotic structure consisting of a core element as restoring force, referred to as neutral fiber, a single SMA actuator wire, and spacer disks. a) The idle state of the structure,[11,42] b) the activated state with fully actuated SMA wire for a continuously guided SMA actuator.[11,42] c) The continuum robotic structure with a partially constraint SMA actuator wire (red), while d) highlights one single section bounded by two spacer disks.

and 2) The only involved forces and moments are due to the SMA wires and the superelastic backbone, with no further additional forces (e.g., friction between SMA and spacer disks, external loads).

In this section, the kinematic model of an ideally guided actuator is considered first. As a result of the constant curvature assumption, the distance between the actuator and the neutral fiber of the core element remains constant while the structure undergoes bending. In the second step, the partial actuator guiding using a certain number of spacer disks, and therefore a nonconstant distance between actuator and neutral fiber is taken into account. The model describes the deviation of the maximum output angle between a fully guided and partially guided actuator based on the number of spacer disks, giving an information on how many spacer disks are required to assume a constant distance between actuator and neutral fiber of the structure. In this

way a practical implementation of a constant curvature bending kinematics is achieved. Lastly, the static equilibrium between the superelastic NiTi core element and the SMA actuator wire is derived, leading to a complete model which is later used to assist the design of SMA-based continuum robots.

2.1. Ideal Constant Curvature Kinematics

For in-plane bending with one single actuator wire, Figure 3 shows the ideal schematic of the continuum robotic system in an idle state (Figure 3a) and in the maximum bent position (Figure 3b). Ideal means that the distance between the SMA wire and the core element remains constant, even though the structure bends.

In an idle state, the length of the superelastic NiTi core element equals the length of the SMA wire. In this position, the continuum robot is in a force-free state and the SMA wire is prestrained by ε_{pre}. When the SMA wire contracts as a result of the Joule heating induced by an electric current, the robotic structure bends in-plane (see Figure 3b). The kinematic relations between the maximum bending angle α, the curvature radius r, continuum robot length L_{NF}, and the distance between SMA wire and neutral fiber d is derived in the following. Here, the guiding of the SMA wires is assumed to be ideal, i.e., it follows the robot curvature radius. The length of the neutral fiber L_{NF} can be described as follows

$$L_{NF} = L_{SMA,OFF} \tag{1}$$

$$L_{NF} = \alpha r \tag{2}$$

$L_{SMA,OFF}$ describes the length of the prestrained and nonactivated SMA wire, while $L_{SMA,ON}$ refers to the maximum contraction of the wire working against the superelastic NiTi rod. $L_{A,SMA}$ describes the austenitic length of the SMA wire, representing the physically minimum achievable length without applying any external forces to the wire (i.e., zero strain state). $L_{SMA,ON}$ refers to the maximum bending of the continuum robot and is defined by ε_{min}, which results from the force equilibrium of the SMA wire and the elastic core element.

$$L_{SMA,ON} = L_{A,SMA}(1 + \varepsilon_{min}) \tag{3}$$

$$L_{SMA,OFF} = L_{A,SMA}(1 + \varepsilon_{pre}) \tag{4}$$

Substituting (4) in (3) and considering the relations in (1) and (2) yields

$$L_{SMA,ON} = \alpha r \frac{1 + \varepsilon_{min}}{1 + \varepsilon_{pre}} \tag{5}$$

The distance d between SMA actuator and the core element is a decisive design parameter to achieve, e.g., a target bending angle α or curvature radius r for a given maximum strain of shape memory alloys. The relationship between these parameters is given by the following equations

$$L_{SMA,ON} = \alpha(r - d) \tag{6}$$

Equating (5) and (6) and solving for r provides the explicit dependency of r on d as well as the prestrain ε_{pre} and minimum strain of the SMA wire ε_{min}, i.e.

$$r = \frac{d}{1 - \frac{1+\varepsilon_{min}}{1+\varepsilon_{pre}}} \tag{7}$$

For in-plane bending, the five free parameters appearing in (1) and (7) can be divided into design parameters ε_{pre}, d, and L_{NF} and performance parameters r and α.

2.2. Approximation of the Constant Curvature Kinematics

The constant curvature kinematics assumes a constant distance between the SMA wire and the core element of the robot, i.e., the SMA wire follows the robot curvature radius. To provide a practical approach toward the theoretical constant curvature kinematics, a robot design with spacer disks is considered, which are equally distributed along the robot backbone. These disks guide the wire and keep it in a defined distance to the core element, see Figure 3c.

Extending the ideal constant curvature kinematic approach by the number of spacers, and considering the fact that the distance between the SMA wire and the core element changes while the structure bends as shown in Figure 3c,d, the following relations result.

Using standard geometric arguments, we obtain

$$L_{SMA,ON} = (L_{NF} - \alpha d) \, \text{sinc}\left(\frac{\alpha}{2n_{sections}}\right) \tag{8}$$

Comparing the maximum output angle for the ideal consideration α_i discussed in Section 2.1 (see Equations (2), (5) and (6)) and the nonideal setup α_{ni} (see Equation (8)), the deviation to the ideal constant-curvature consideration can be calculated depending on the number of spacers, and is given by substituting (2) and (6) in (8)

$$\frac{\alpha_i}{\alpha_{ni}} = \frac{L_{NF}}{\alpha_{ni}d}\left[1 - \text{sinc}\left(\frac{\alpha_{ni}}{2n_{sections}}\right)\right] + \text{sinc}\left(\frac{\alpha_{ni}}{2n_{sections}}\right) \tag{9}$$

Figure 4 shows the dependency between the ratio $\frac{\alpha_{ni}}{\alpha_i}$ and the number of sections. To achieve a deviation of the output angle of less than 1%, indicated by the black dotted line, a minimum of 11 spacers is required, i.e., 10 sections. Here, $d = 4\,\text{mm}$ and $L_{NF} = 100\,\text{mm}$ are chosen, while the number of sections is varied from 1 to 15.

2.3. Quasi-Static Force Equilibrium for Single SMA Continuum Robots

After deriving the kinematic relationships, a suitable SMA wire needs to be chosen by accounting for its force performance. Assuming negligible friction between actuator and spacers, as well as the absence of external forces, the bending moment M, which needs to be generated by the SMA wire to bend the continuum robot with its elastic core element, is given by the following relationship[35]

$$M = IE_{core}\kappa \tag{10}$$

where I and E_{core} describe the second moment of area and the Young's modulus of the NiTi rod, respectively, while $\kappa = \frac{1}{r}$ describes the curvature of the core element. The corresponding force is given by
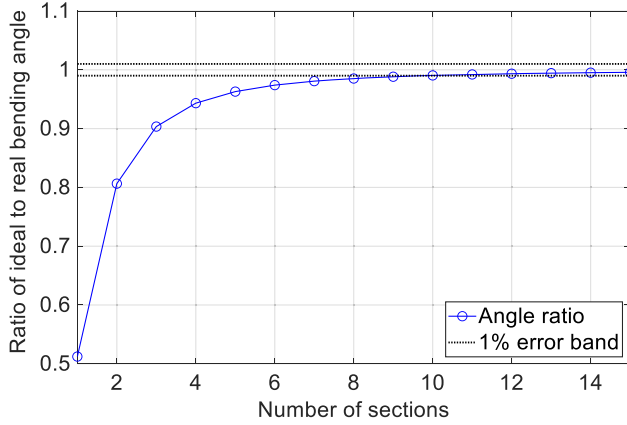
Figure 4. Deviation of the maximum bending angle between a partially guided and a fully guided actuator based on the number of spacer disks, including an error band of 1% (black dotted line).

$$F = \frac{IE_{core}\kappa}{d} \tag{11}$$

with $\alpha = L_{NF}\kappa$ and $\alpha = \frac{L_{NF}\varepsilon}{d}$, where ε describes the strain of the SMA wire, Equation (11) can be rewritten as

$$F = \frac{IE_{core}}{d^2}\varepsilon \tag{12}$$

Thus, for the planar bending case, the mechanical load that the SMA wire needs to overcome simplifies to a 1D model linear spring, as also described in refs. [34,38]. This force equilibrium can be solved graphically, as common in SMA-spring actuator designs.[25] To achieve the maximum bending angle, the pre-strain ε_{pre} is set to the maximum strain of the wire without generating any force on the elastic rod, since this would cause an undesired bending of the continuum robot in an idle state. As shown in **Figure 5**, this strain equals to ε_T. To determine the maximum possible bending angle, the minimum achievable SMA wire strain ε_{min} needs to be calculated given by the force equilibrium of the austenitic SMA wire and the elastic rod, which is defined as

$$F_{SMA} = -F_{core} \tag{13}$$

When the SMA wire contracts at its minimum possible length, a fully austenitic state as shown in Figure 5 is assumed. Therefore, the SMA wire force can also be approximated as a line based on the austenite Young's modulus $E_{A,SMA}$, the cross-sectional area $A_{cross,SMA}$, and the wire strain ε.

$$F_{SMA} = \sigma_{SMA} * A_{cross,SMA} = \varepsilon * E_{A,SMA} * A_{cross,SMA} \tag{14}$$

The force of the core element results from Equation (12), where the strain of the SMA wire is defined as the difference between prestrain and current strain state.

$$F_{core} = \frac{IE_{core}}{d^2}(\varepsilon - \varepsilon_{pre,SMA}) \tag{15}$$

Substituting (14) and (15) into (13) and rearranging to ε yields
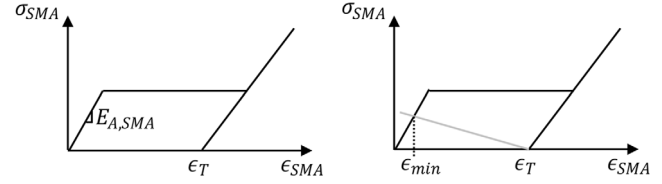
Figure 5. Stress–strain characteristics of an SMA wire working against a spring. The black curve indicates the characteristic stress–strain hysteresis of an SMA wire, while the gray line represents the stress–strain characteristics of a linear spring.

$$\varepsilon = \varepsilon_{pre,SMA} * \frac{1}{\frac{d^2 * E_{A,SMA} * A_{cross,SMA}}{IE_{core}} + 1} \tag{16}$$

with $\varepsilon = \varepsilon_{min}$ and $\varepsilon_{pre,SMA} = \varepsilon_T$, Equation (16) defines the minimum achievable strain of the SMA wire. Together with the pre-strain, the maximum possible strain change of the SMA wire can be derived, defining the maximum robot bending angle, as depicted in Equation (5).

2.4. Quasi-Static Force Equilibrium for Three SMA Continuum Robots

For spatial bending of a continuum robot, at least three SMA wire actuators are needed. As described in ref. [11], the wires are placed at a defined distance to the neutral fiber of the continuum robot, being arranged on a circumference with an offset of 120° to each other (see **Figure 6**b, left). By either actuating a single SMA wire or two SMA wires simultaneously, the bending direction of the continuum robot can be controlled. Actuating one single SMA wire, bends the continuum robot in the direction of this wire, while actuating two SMA wires with the same current results in a bending motion of the robot along the direction opposite to the one of the passive SMA wire, as shown exemplary in Figure 6a,b. Compared to the single SMA wire continuum robot for planar bending, in this case each of the three SMA wires can now change their length upon activation. This in turn enables an elongation of each single SMA wire above its prestrain when the opposing wires are activated. To limit the maximum strain to ε_T, the prestrain and therefore the minimum achievable strain of each single-actuated SMA wire change compared to the single SMA considerations. The SMA wire strain can be calculated based on the equations in ref. [39] for tendon-driven continuum robots considering the constant curvature kinematics.

$$\varepsilon_{pre,SMA} = \frac{\varepsilon_{SMA1} + \varepsilon_{SMA2} + \varepsilon_{SMA3}}{3} \tag{17}$$

$$\frac{\varepsilon_{pre}}{\varepsilon_T + \varepsilon_{min}} = 0,5 \tag{18}$$

Defining the prestrain as the mean value between the minimum strain ε_{min} and the maximum strain ε_T, the minimum achievable strain can be calculated by rearranging (18) and substituting into (16), yielding
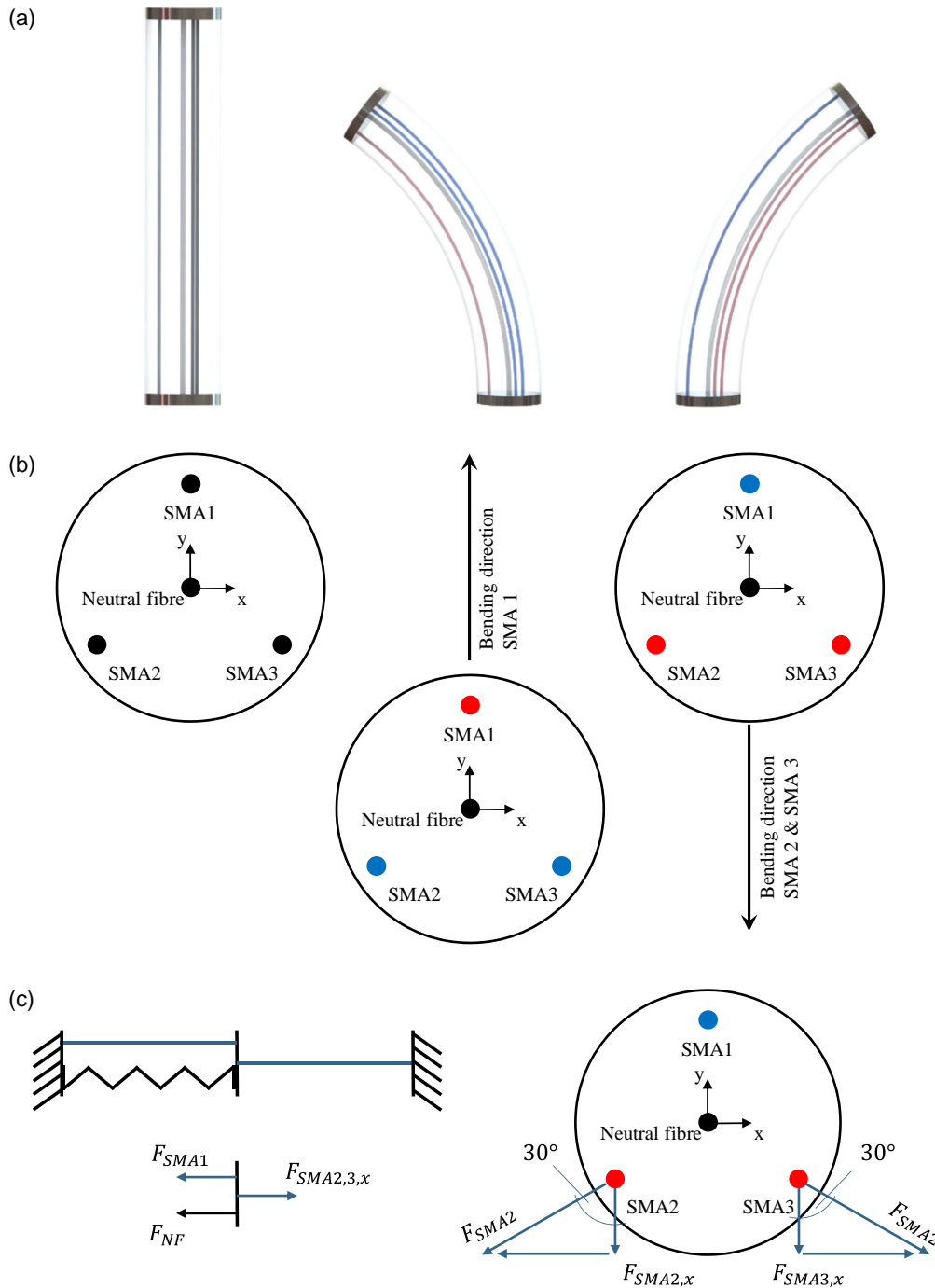
Figure 6. 3D sketch a) and the top view b) of a continuum robot consisting of an elastic backbone and three SMA actuator wires, indicating the bending direction when actuating SMA1 as well as the bending direction when actuating SMA2 and SMA3 simultaneously and equally. A simplified 1D model illustrates the force equilibrium as well as the force contribution in this case c). The black-colored dots display SMA wires in idle state, while the red dots indicate activated (and thus contracted) SMA wires, and the blue dots represent the passively elongated SMA wires.

$$\varepsilon_{\min} = \varepsilon_{\mathrm{pre,SMA}} * \frac{1}{\frac{2*d^2*E_{\mathrm{A,SMA}}*A_{\mathrm{cross,SMA}}}{IE_{\mathrm{core}}} + 1} \tag{19}$$

These equations yield the minimum achievable strain for a single wire being actuated as for example SMA1 shown in Figure 6b, center which then leads to the corresponding maximum bending

angle. Besides the maximum contraction for a single wire, the second extreme is described by its maximum possible elongation due to a contraction of the other wires. Sticking with SMA1, actuating SMA2 and SMA3 simultaneously results in a minimum strain $\varepsilon_{\mathrm{min,SMA2,3}}$ of both wires, causing a bending movement

of the structure in the direction shown in Figure 6b right. This scenario represents the maximum elongation case for SMA1 and can be calculated correspondingly for all three wires. To determine $\varepsilon_{\mathrm{min,SMA23}}$, the force equilibrium from Section 2.3 is extended taking all three wires into account (see Figure 6c).

Based on the force equilibrium along the y-axis, see Figure 6c, the following equations determine the minimum strain $\varepsilon_{\mathrm{min,SMA23}}$ for the wires SMA2 and SMA3, which cause the maximum elongation in SMA1

$$F_{\mathrm{NF}} + F_{\mathrm{SMA1}} = F_{\mathrm{SMA2,3},x} \tag{20}$$

The force components are calculated as follows.

$$F_{\mathrm{NF}} = \frac{IE}{d^2}(\varepsilon_{\mathrm{pre,SMA}} - \varepsilon_{\mathrm{min,SMA23}}) \tag{21}$$

$$F_{\mathrm{SMA1}} = E_{\mathrm{M,SMA}} * A_{\mathrm{cross,SMA}} * (\varepsilon_{\mathrm{SMA1}} - \varepsilon_{\mathrm{T}}) \tag{22}$$

$$_{\mathrm{SMA2,3},x} = \sqrt{3} * E_{\mathrm{A,SMA}} * A_{\mathrm{cross,SMA}} * \varepsilon_{\mathrm{min,SMA23}} \tag{23}$$

The strain of SMA1, namely, $\varepsilon_{\mathrm{SMA1}}$, can be calculated rearranging Equation (17). In the discussed case where SMA2 and SMA3 are actuated equally and simultaneously, the resulting strain of these wires is equal to the minimum strain $\varepsilon_{\mathrm{min}}$.

$$\varepsilon_{\mathrm{SMA2}} = \varepsilon_{\mathrm{SMA3}} = \varepsilon_{\mathrm{min,SMA23}} \tag{24}$$

Substituting (21)–(23) into (20) and solving for $\varepsilon_{\mathrm{min}}$ leads to the following equation

$$\varepsilon_{\mathrm{min,SMA23}} = \frac{\frac{IE}{d^2} * \varepsilon_{\mathrm{pre,SMA}} + E_{\mathrm{M,SMA}} * A_{\mathrm{cross,SMA}} * (3 * \varepsilon_{\mathrm{pre,SMA}} - \varepsilon_{\mathrm{T}})}{\frac{IE}{d^2} + 2 * E_{\mathrm{M,SMA}} * A_{\mathrm{cross,SMA}} + \sqrt{3} * E_{\mathrm{A,SMA}} * A_{\mathrm{cross,SMA}}} \tag{25}$$

The maximum resulting elongation strain of SMA1 can be calculated as follows

$$\varepsilon_{\mathrm{SMA1,max}} = \varepsilon_{\mathrm{SMA1}} + \varepsilon_{\mathrm{T}} \tag{26}$$

Figure 7 illustrates the stress–strain characteristics as well as the force equilibrium described in (20) and thus the resulting minimum achievable strain derived in Equation (25), when actuating two SMA wires equally and simultaneously causing an elongation of the passive wire SMA1.

To provide a design guide derived from the presented model to systematically obtain the target performance of an SMA-driven continuum robot, an example is given using a set of predefined parameters. Assuming a given length of the robot backbone, a given core element diameter and SMA wire diameter as well as a given SMA wire prestrain of ε_{T} and a desired maximum bending angle for a single SMA continuum robot, first the minimum achievable strain needs to be defined using Equation (16). Then, Equations (3)–(6) solve for the two parameters r and d. Finally, the number of spacer disks needs to be calculated for a given maximum deviation to the constant curvature kinematics using Equation (9). Following this procedure, all required design as well as performance parameters are defined.
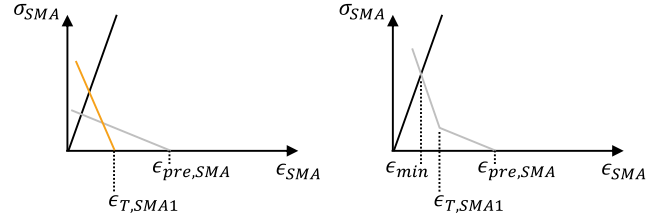
Figure 7. Stress–strain characteristics of two SMA wires working against a spring and a passive SMA wire. The black curve indicates the elastic austenitic branch of the stress–strain hysteresis of the two actuated SMA wires, the gray line in the left diagram indicates the stress–strain characteristics of a linear spring, and the yellow line represents the elastic martensitic branch of the stress–strain hysteresis of the passively elongated SMA wire. The resulting equilibrium gives the minimum achievable strain as well as the resulting stress for such a setup.

3. Experimental Section

To validate the general constant curvature model for continuum robots excluding the SMA characteristics as well as the quasistatic coupled models for planar and spatial motion, experimental test rigs are built. The experimental setups as well as the results are presented in this section. First, the constant curvature kinematics is validated in the general case by using a steel wire as actuator element, by considering different design parameters. Second, a single SMA wire planar continuum robot is developed and used to validate the general constant curvature model, together with specific SMA design considerations regarding the wire prestrain (cf. Section 2). Finally, a spatially bending continuum robot with three SMA wires is built to validate the design procedure, in combination with two antagonistically arranged passive SMA wires. All experiments are carried out based on in-plane measurements. Each prototype has a backbone length of 100 mm and an outer diameter of 20 mm defined by the diameter of the acrylic spacer disks. As core elements superelastic NiTi rods are used.

3.1. Validation of the General Constant Curvature Model

Figure 8 shows the test rig to validate the constant curvature kinematics using a steel wire from Flexonit with a diameter of 0.45 mm as actuator element. The checkerboard pattern attached to the tip of the continuum robot allows to track the tip displacement using a camera. The continuum robot is fixed on one end, with the tip hanging downward. A steel wire is fixed at the tip of the continuum robot, guided through the equidistantly distributed spacer disks and fixed to a KD24s load cell from ME-Meßsysteme, which in turn is mounted to a linear drive, PS01-23 × 160 H-HP-R from LinMot.

The motor position acts as input, while the load cell measures the required actuator force, and the camera setup tracks the angle of the continuum robot's tip. For each experiment, the motor drives upward by 4 mm corresponding to 4% of the continuum robot length of $L_{\mathrm{NF}} = 100$ mm, and subsequently comes back to its start position. This loading profile forces the robot to bend and relax again. The experiment is performed for different structural parameters of the robot. The corresponding parameters of
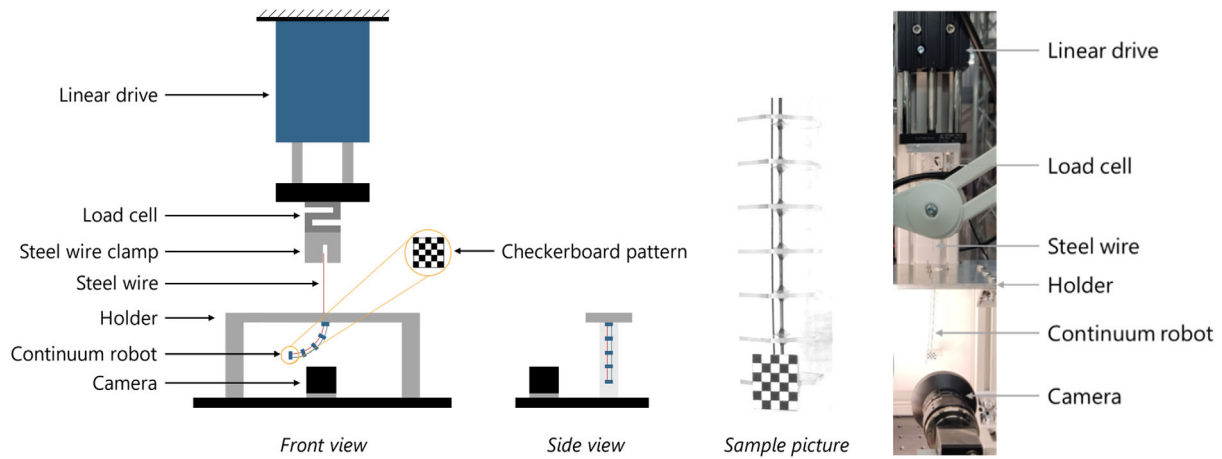
Figure 8. Schematic diagram of the test rig to experimental validate the constant curvature model for continuum robots (left). The test rig consists of a linear motor, a load cell, a camera, and a continuum robot including a steel wire. A sample picture of the continuum robot's tip, together with the checkerboard pattern being used to track the bending angle is shown (center). A photograph of the real setup is shown on the right.

interest, including the tested numerical values, are reported in **Table 2**.

The first parameter being varied is the diameter of the core element d_{core}. The distance between steel wire and core element is chosen to $d = 4$mm and the number of spacer disks is set to $n_{spacer} = 11$. With $\varepsilon_{pre} = 0.04$ and $\varepsilon_{min} = 0$, Equation (7) gives the bending radius $r = 104$mm at maximum bending of the continuum robot. Using Equation (2), the ideal maximum bending angle is calculated to $\alpha = 55°$. To minimize the friction between spacer disks and steel wire, Teflon tube pieces are inserted at the contact points. As indicated in **Figure 9**, there is a clearance between the guiding hole of the spacer disk and the steel wire combined with the Teflon tube. When the continuum robot bends, the steel wire is forced to move to the outer edge of the guiding hole (see Figure 9, right). Accordingly, the distance between steel wire and core element changes from ideal values $\underline{d} = [2;4;6]$mm to

$\underline{d} = [2.2;4.1;6]$mm yielding $r = 106.6$mm and $\alpha = 53.7°$.

The results when varying the diameter of the core element d_{core} are shown in **Figure 10**. The upper part of Figure 10, shows the imposed motor motion, while the bottom-left of the same figure reports the bending angle of the tip over the stroke of the linear drive. The observed trend is in line with what expected from Equation (15). The bottom-left part of Figure 10 shows a small

Table 2. Parameters and respective values being used for the experiments to validate the general constant curvature model.

Parameter	Values
Diameter of the core element d_{core}	0.4 mm
	0.8 mm
	1.2 mm
Distance between steel wire and core element d	2 mm
	4 mm
	6 mm
Number of spacer disks n_{spacer}	11,6,5,4,3,2
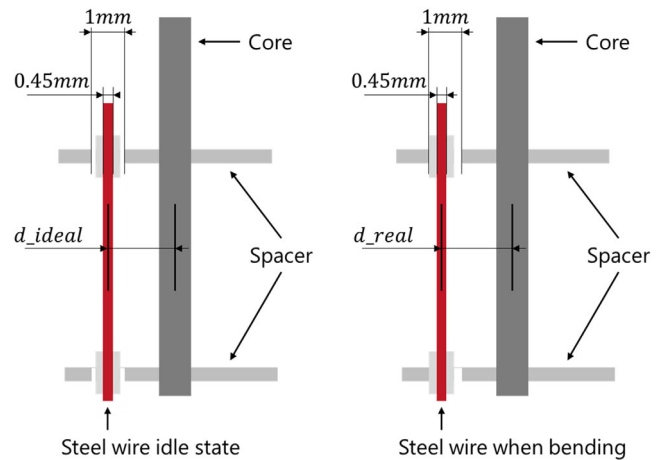
Figure 9. Schematic drawing showing the guiding of the steel wire through the holes within the spacers: the ideal distance between steel wire and core element (left) as well as the worst-case alignment during bending of the continuum robot (right) are illustrated.

deviation of the maximum achievable bending angle. In particular, the thicker the core element the smaller the angle, as a result of the steel wire stiffness. This effect results into higher forces for increasing core diameters, as shown in Figure 10, (bottom right).

The maximum measured bending angle equals to 53.6° for the blue curve and 53.1° for the red curve, respectively, showing a good agreement with the theoretically calculated value of 53.7°. The observed hysteresis in the force–angle curve, visible in Figure 10 (bottom right), is a result of the friction between the steel wire and the spacer disks. As discussed in ref. [40], this phenomenon can be explained as history-dependent friction occurring in partially constrained continuum robots. The maximum required actuator forces calculated according to Equation (12) yield $\underline{F} = [0.27;4.14;13.2]$N, while the measurements equal $\underline{F} = [0.29;4.25;13.4]$N, showing again a good agreement with the theoretical model.
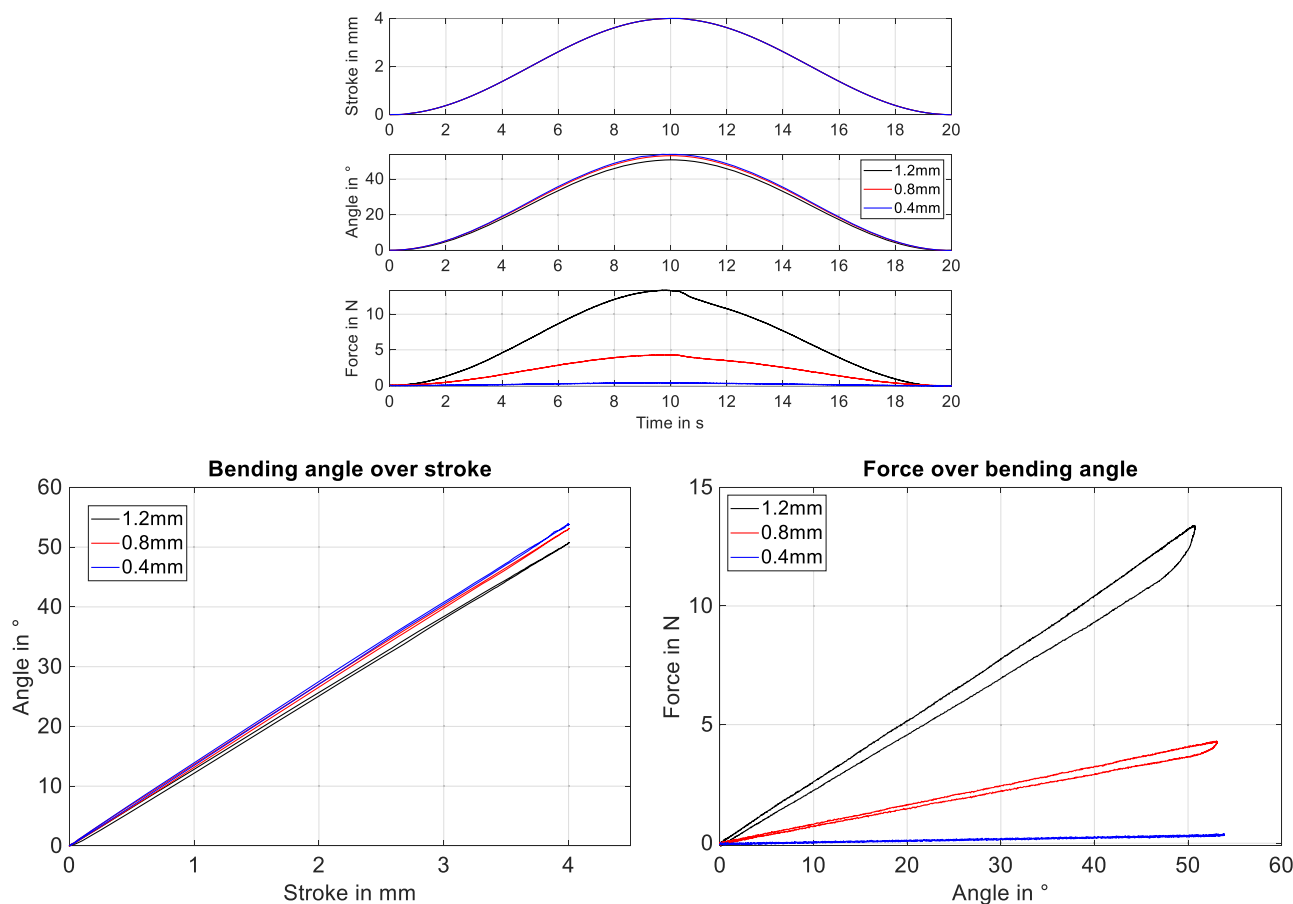
Figure 10. Variation of the elastic core diameter: experimental results for a continuum robot driven by pulling on a steel wire being attached to the continuum robot tip. The displacement of the linear drive as setpoint as well as the resulting measurements of the required actuator force and the bending angle of the tip are shown.

In the second experiment, the distance between the steel wire and the core element is varied, keeping the core diameter constant at $d_{core} = 0.8$mm. The results are shown in **Figure 11**. As expected, the bending angle as well as the required actuator force decreases with increasing distance d. The calculated and measured values are given in **Table 3**.

These two parameter variations validate the constant curvature kinematics using 11 spacer disks, without accounting for the SMA behavior. The variation of the number of spacer disks in additional experiments provides information on how many spacer disks are required to meet the constant curvature kinematics model. Keeping the core diameter constant at $d_{core} = 0.8$mm and the distance between steel wire and core element at $d = 4$mm, **Figure 12** shows that using 4 spacer disks provides a good approximation of the constant curvature kinematics with a deviation of 6.4% from the ideal case, while 6 spacer disks result in deviations of about 3% (see Table 3).

3.2. Characterization of SMA Wires

When designing a continuum robot based on SMA wire actuators, their limited strain needs to be considered as well as the

force equilibrium of the actuator and the elastic core element, acting as a linear restoring spring (see Figure 5b). As described in Section 2, the idle position of the continuum robot refers to a force-free state, limiting the maximum prestrain of the SMA wire when being attached to the robot structure to ε_T. For a single wire continuum robot, the minimum achievable strain is given by Equation (16), where the austenitic Young's modulus as well as an appropriate diameter of the SMA wire need to be known. To be able to identify these parameters, the test rig shown in Figure 8 is modified as shown in the following schematic drawing by fixing the lower end of the SMA wire to a rigid plate (**Figure 13**). The experimental characterization allows for extracting the relevant material parameter, such as Young's modulus as well as the remanent strain, without having to know details on the material composition or processing.

To characterize the SMA wire mechanically, austenitic tensile tests are carried out. A single batch of SMA wires from SAES Getters is used in all experiments. For the given material, a transformation temperature of $A_s = 90°$C is expected. For each experiment, the wire is heated with a constant electric power while the linear drive elongates the wire up to 5% strain, according to a sinusoidal profile at a frequency of 0.05Hz. The characterized
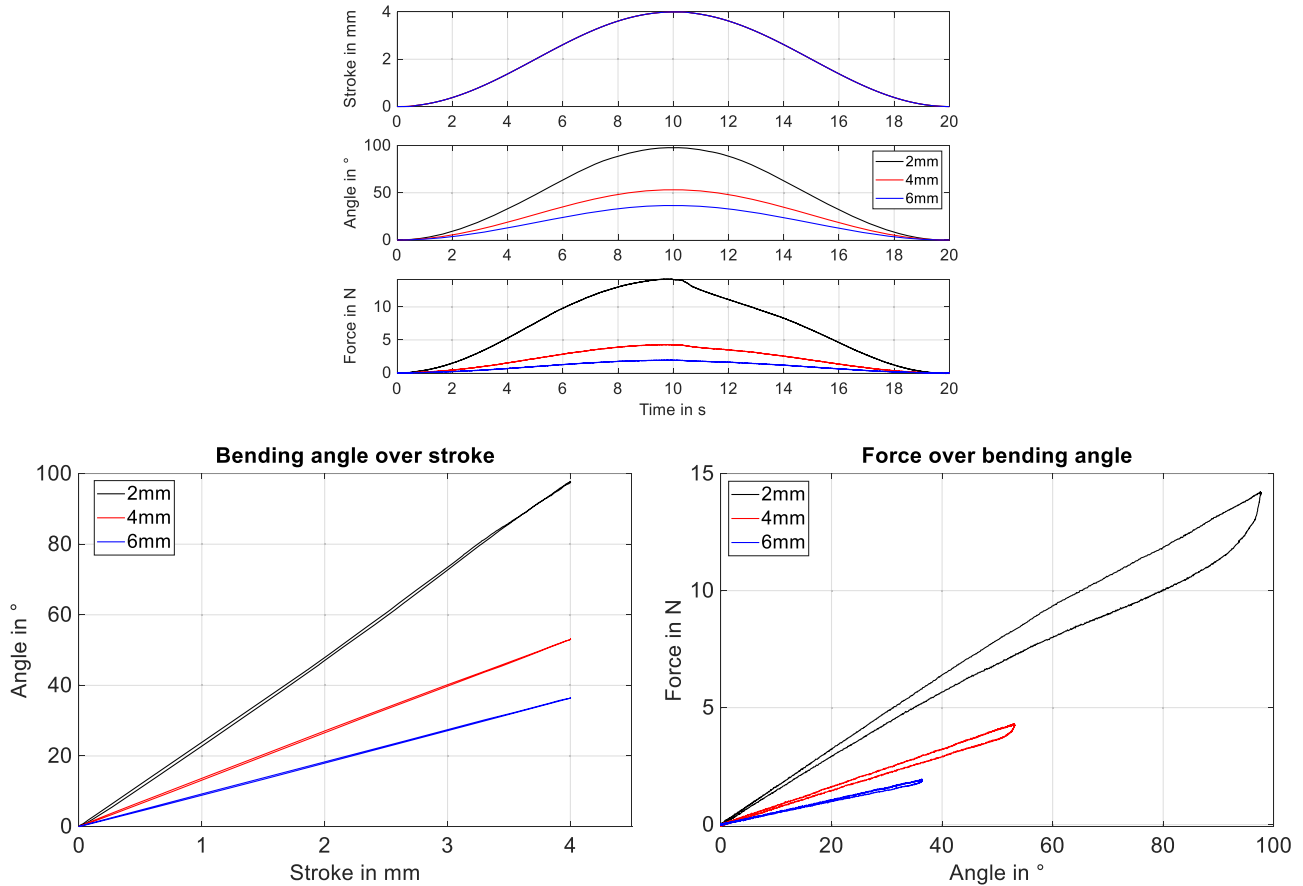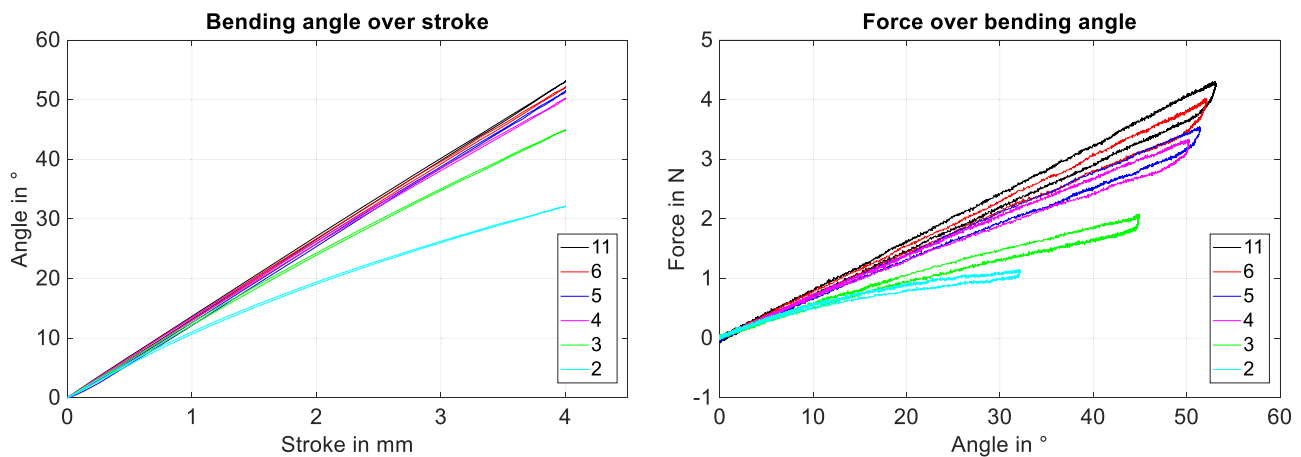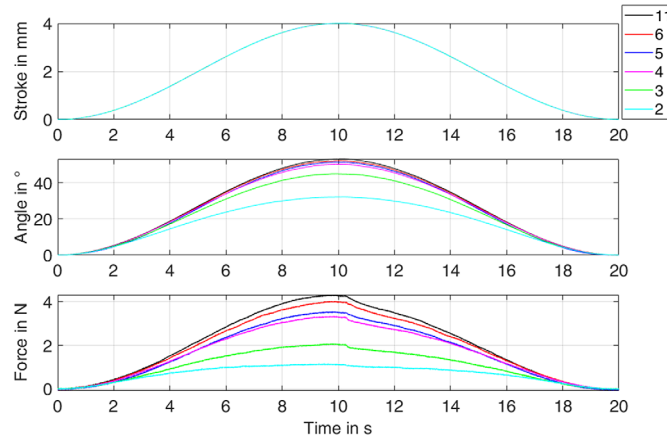
Figure 11. Variation of the distance between core element and steel wire as actuator element: experimental results for a continuum robot driven by pulling on a steel wire being attached to the continuum robot's tip. The displacement of the linear drive as setpoint as well as the resulting measurements of the required actuator force and the bending angle of the tip are shown.

Table 3. Theoretical and measured values for the maximum bending angle and the maximum required actuator force varying the diameter of the elastic core element d_{core}, the distance between steel wire as actuator element and elastic core d, and the number of spacer disks n_{spacer}. The deviations of calculated and measured values are given in the right column.

| Experiment	Calculated value	Measured value	Error
Variation of d_{core}	$\alpha = 53.7°$	$\alpha = [53.6; 53.1; 50.7]°$	$e = [0.2; 1.1; 5.6]\%$
	$F = [0.27; 4.14; 13.2]N$	$F = [0.29; 4.25; 13.6]N$	$e = [5.6; 2.66; 3]\%$
Variation of d	$\alpha = [100; 53.7; 36.7]°$	$\alpha = [97.7; 53.1; 36.5]°$	$e = [2.3; 1.1; 0.55]\%$
	$F = [14.33; 4.04; 1.84]N$	$F = [14.2; 4.25; 1.92]N$	$e = [0.8; 5.2; 4.3]\%$
$n_{spacer} = 4$	$\alpha = 53.7°$	$\alpha = 50.24°$	$e = 6.4\%$
$n_{spacer} = 6$	$\alpha = 53.7°$	$\alpha = 52.2°$	$e = 2.8\%$
	$F = 4.14 N$	$F = 4 N$	$e = 3.4\%$

austenitic SMA wire length is set to 100mm and has a diameter of 150µm. First, the SMA wire is heated up without applying a mechanical stress, to let it fully transform to austenite. The black curve in **Figure 14** represents the mechanical response of the wire after it has been cooled down at room temperature of 22°C. The red curves show the results of the same tensile test, carried out after the tensile test shown by the black curve without

any additional heating of the wire. In the third experiment, the wire is heated up using a constant electric power of 600mW (blue curve in Figure 14). Based on the blue curve, the austenitic Young's modulus of the SMA wire is estimated to be 45GPa. The minimum achievable strain can be calculated based on Equation (16). Consequently, it results in $\varepsilon_{min} = 0.48\%$ for the following setup: $d = 4.1mm$, $d_{core} = 0.8mm$, $E_{core} = 90GPa$,

Figure 12. Variation of the number of spacers: experimental results for a continuum robot driven by pulling on a steel wire being attached to the continuum robot tip. The displacements of the linear drive are shown, alongside the resulting measurements of the required actuator force and the bending angle of the tip.
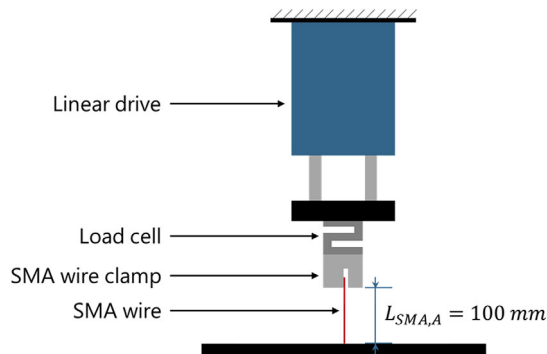
Figure 13. Schematic drawing of the test rig used to characterize the mechanical characteristics of SMA wires. The SMA wire is fixed to a non-moving plate on one end and to a load cell on the other end. Both wire ends are electrically connected. The load cell is attached to a linear drive which is used to elongate the wire while being heated using different constant power values.

$d_{SMA} = 150\,\mu m$, $E_{A,SMA} = 45\,GPa$, and $\varepsilon_{pre,SMA} = \varepsilon_T = 4\%$. The intersections between spring and SMA characteristics, highlighted with a red circle in Figure 14 (bottom right) give

a minimum strain of $\varepsilon_{min} = 0.5\%$ and an error of 4% compared to the calculated value, accordingly.

3.3. Validation of the General Constant Curvature Model with Single SMA

Based on Equations (2) and (7), the maximum bending angle for a single SMA-driven continuum robot is given as $\alpha = 47.3°$, with a corresponding curvature radius at maximum bending of $r = 121\,mm$. To validate these calculations, and thus the combination of the constant curvature kinematics with the SMA wire characteristics, a single SMA wire continuum robot is built and characterized. The modifications of the test rig illustrated in Figure 8 are shown in **Figure 15**.

While one end of the SMA wire is glued to the spacer disk at the tip of the continuum robot, the other end is mechanically fixed to a load cell to measure the force generated by the actuator wire. Electrically connecting the wire at both ends allows for activating the SMA wire using different power signals as input signals, resulting in heating up and contracting the wire and thus bending of the continuum robot. Also in this case, a camera is used to measure the angle of the tip. **Figure 16** (left) shows the input signal, a
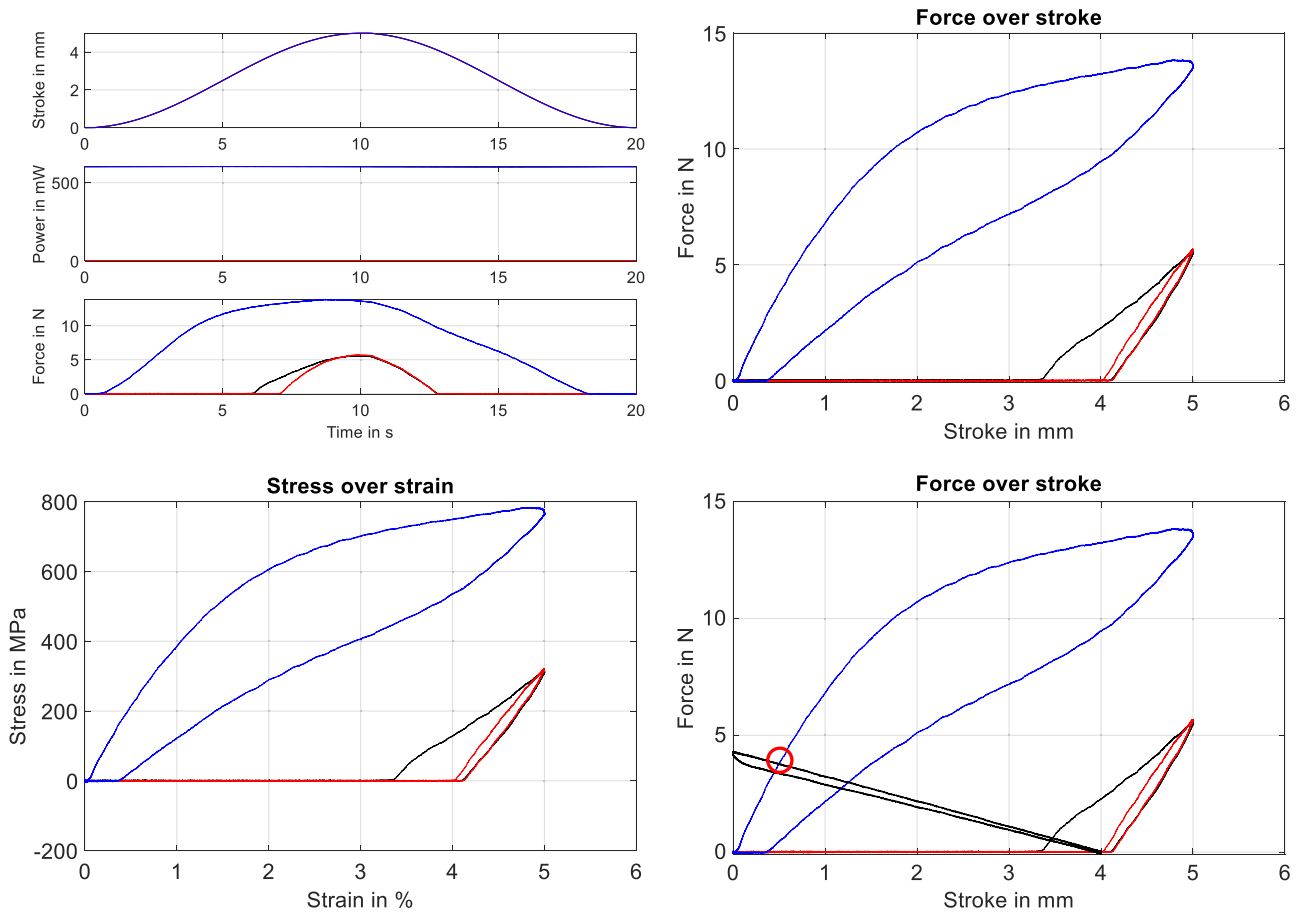
Figure 14. Experimental results of the SMA wire characterization using a wire with a diameter of 150 µm. The wire is electrically powered using different constant power values. At the same time, the linear drive is pulling on the SMA wire. Bottom right shows the force equilibrium (red circle) of the SMA wire and the continuum robotic structure, and thus giving a graphical method to determine the minimum strain ε_{min}.
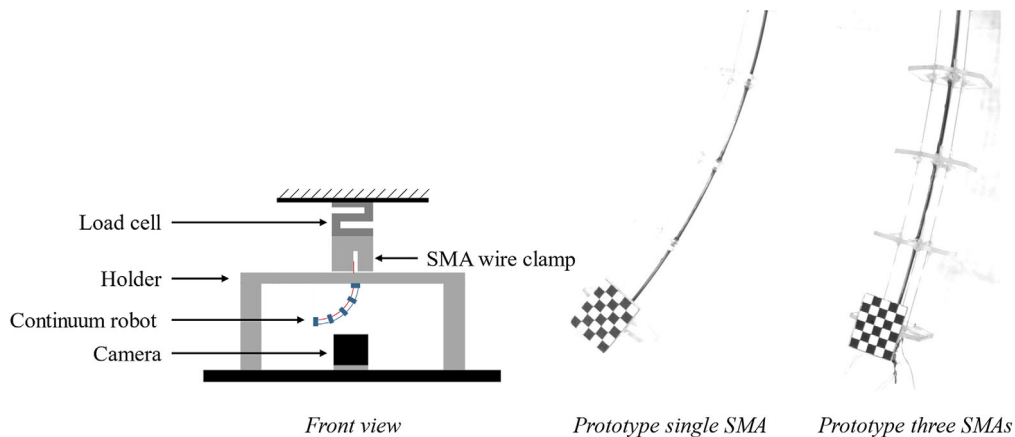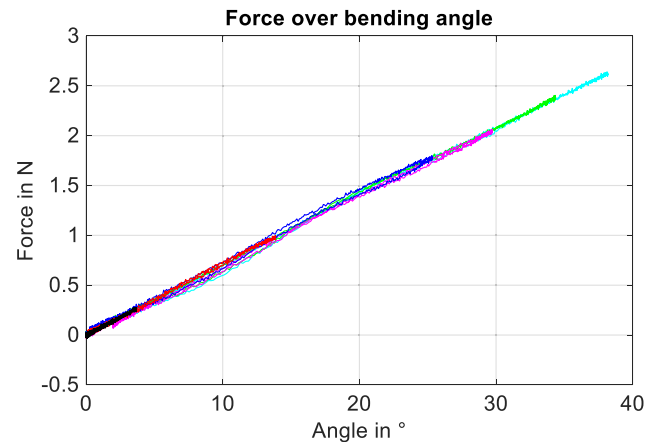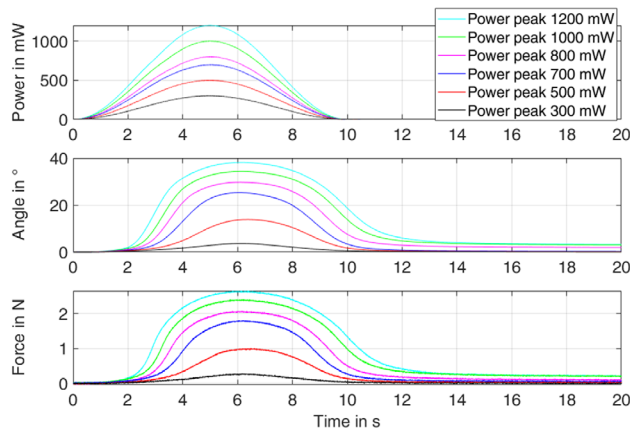

Figure 15. Test rig allowing for measuring the actuator force as well as the bending angle of the continuum robot for SMA-driven continuum robots (left). The prototypes with a single-integrated SMA wire (center) and three-integrated SMA wires (right).

sinusoidal power setpoint, as well as the resulting angle and force for different maximum power amplitudes.

The maximum achievable force of an SMA wire and thus the maximum bending angle of the continuum robot tip depends on the supplied input energy. Therefore, the maximum bending angle increases with increasing power amplitudes, keeping the heating time constant to 10s. To increase the energy input within the heating time, experiments with a different input power signal

2301502 (13 of 17)

**ADVANCED
SCIENCE NEWS**

www.advancedsciencenews.com

**ADVANCED
ENGINEERING
MATERIALS**

www.aem-journal.com

Figure 16. Experimental results for an in-plane bending of a single SMA wire-driven continuum robot using sinusoidal power inputs.

are performed, as shown in **Figure 17** (left). As expected, there is still a linear dependency between the tip angle and the actuator force, see Figure 16 (right). The maximum bending angle achieved with a ramp input power with a maximum power of $P = 1.2$W and a holding phase of 90% results in $\alpha = 46.3°$. Compared to the theoretically calculated bending angle of 47.3°, the corresponding error equals 2.11%.

3.4. Validation of the General Constant Curvature Model with Three SMAs

Based on Equation (19), the minimum achievable strain of the SMA wires changes compared to the planar, single-actuator case. Using the same continuum robot parameters, it results in $\varepsilon_{min} = 0.25\%$, leading to a prestrain of $\varepsilon_{pre} = 2.125\%$, according to (18). A graphical validation provides a minimum strain of $\varepsilon_{min} = 0.265\%$, highlighted with a red circle in **Figure 18**, amounting to an error of e = 5.7%.
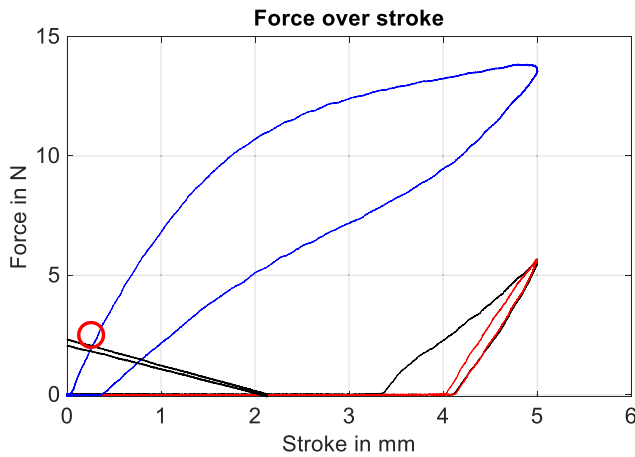
The extreme cases for a single SMA wire are represented by its maximum contraction and its maximum elongation. The former results from the actuation of the corresponding SMA wire itself, while the latter yields by actuating the two opposing SMA wires equally and simultaneously. To validate the model for these cases, experiments are conducted using the test rig shown in Figure 15. Additionally, two SMA wires with an offset of 120° are integrated in the continuum robotic structure, see Figure 6 and 15 (right). **Figure 19** (top) shows the results for activating one single SMA wire, while the opposing SMA wires are passive. The wires are prestrained to $\varepsilon_{pre} = 2.1\%$ and, based on the calculated minimum achievable strain of $\varepsilon_{min} = 0.25\%$, a maximum bending angle of 25.36° is expected. The measurements show a maximum bending angle of 25.2°, resulting in an error of 0.63%. Based on Equation (17), the two opposing wires will be elongated to 3.06%. Taking into account that the SMA wires are only generating an opposing force at strains larger than $\varepsilon_T = 4\%$, the force equilibrium simplifies to the 1D model shown in Figure 5. Thus, the resulting force of the actuated SMA wire is supposed to exhibit the linear spring characteristic of the superelastic core element, as confirmed by the measurements illustrated in Figure 19 (top right).

The experimental results regarding the maximum elongation of the same wire, caused by the actuation of the opposing wires are
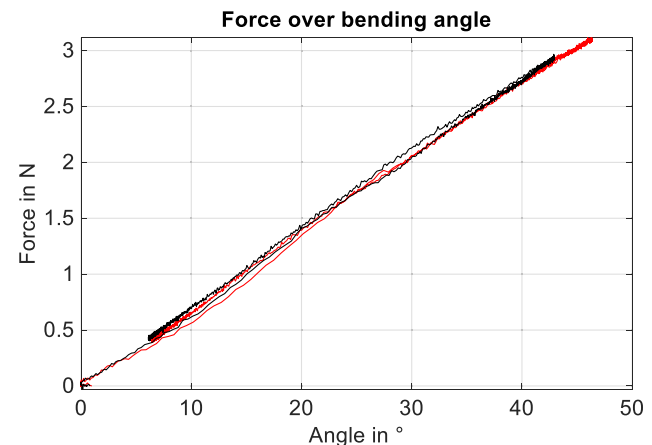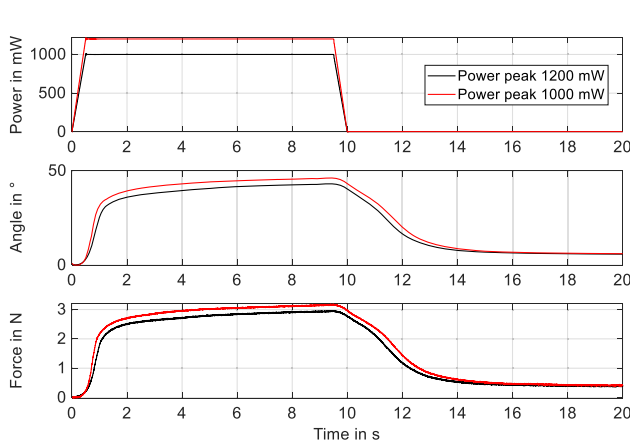
Figure 17. Experimental results for an in-plane bending of a single SMA wire-driven continuum robot using power inputs with a ramp waveform.

**ADVANCED
SCIENCE NEWS**

www.advancedsciencenews.com

**ADVANCED
ENGINEERING
MATERIALS**

www.aem-journal.com

Figure 18. Force equilibrium (red circle) of the SMA wire and the continuum robotic structure for an SMA wire prestrain $\varepsilon_{\text{pre,SMA}} = 2.125\%$. The graphical solution leads to a minimum achievable strain of $\varepsilon_{\text{min}} = 0.265\%$.

shown in Figure 19 (bottom). For these experiments, each SMA wire is driven by a separate constant current source. For an SMA prestrain of $\varepsilon_{\text{pre,SMA23}} = 1.54\%$, the minimum achievable

strain equals to $\varepsilon_{\text{min}} = 0.26\%$, resulting in a maximum theoretical bending angle of 30.5° and a maximum force of the passive, elongated SMA wire of 2.47 N. The measurements show a maximum bending angle of 31.66° and a maximum force of 2.41 N, with corresponding errors of 3.7% and 2.7%, respectively. Since the continuum robotic structure bends toward the opposite direction, the bending angle is negative. Measuring the force of the passive SMA wire, a linear elastic force-stroke and thus force-angle characteristic is expected, when the wire is being elongated above $\varepsilon_T = 4\%$, see Figure 7. Figure 19 (bottom) confirms the model and shows that the passive wire is elongated above ε_T at a bending angle of 23°.

There are two ways to avoid elongating the passive SMA wire above ε_T, which in turn permits drastically increasing the wires lifetime. Those possibilities consist of either reducing the prestrain of all three wires, resulting in a reduced maximum bending angle and workspace of the continuum robot, respectively, or using strain feedback in conjunction with a closed loop control algorithm to prevent elongating the wires to elongate over a defined length, while keeping the maximum workspace of the continuum robot. The latter solution can be achieved using the inherent self-sensing capability of SMA wires, which can be directly related to their strain.[28] This approach, although
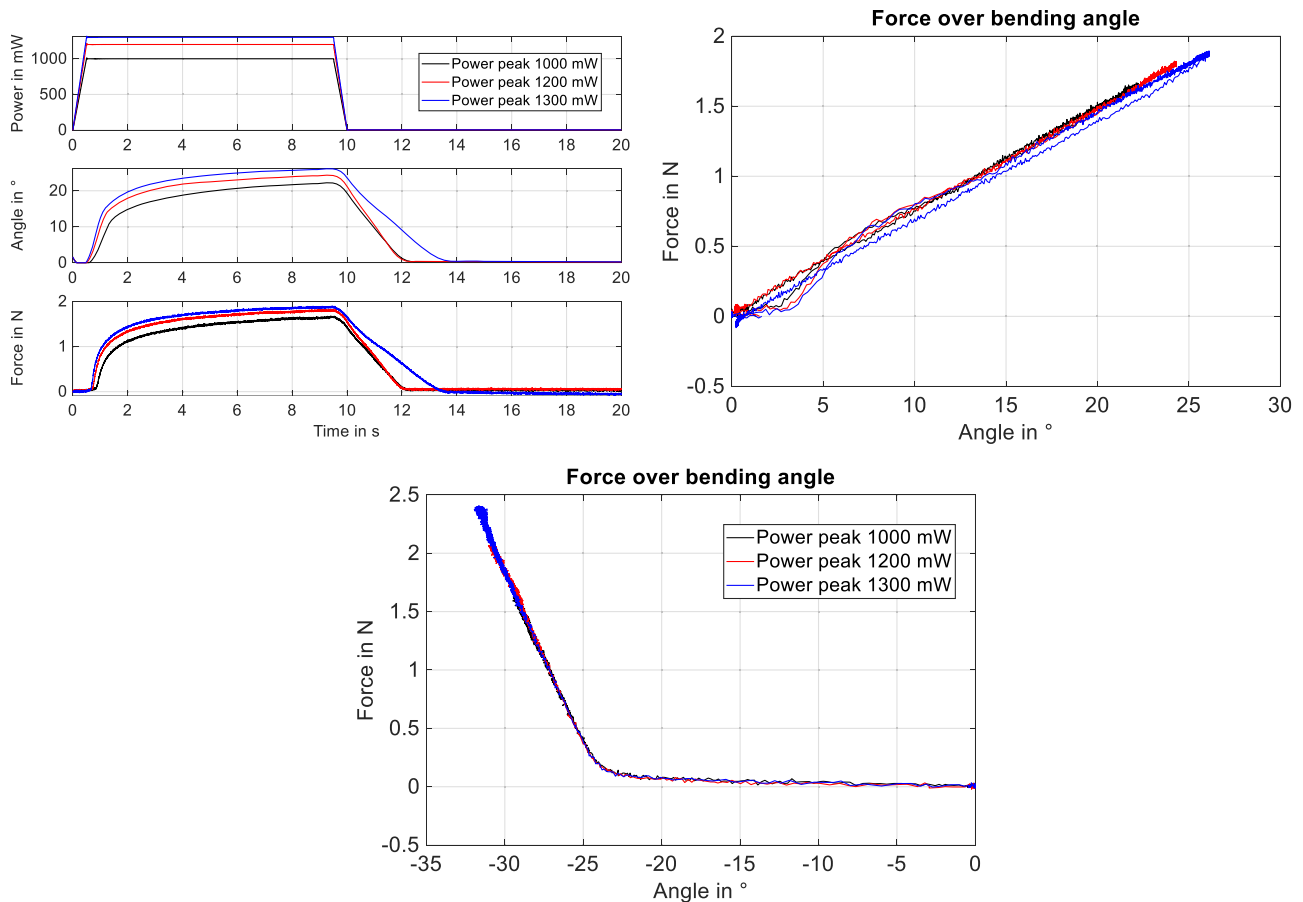
Figure 19. Experimental results for an in-plane bending of an SMA wire-driven continuum robot with three SMA wires. Top left shows the power for SMA1 and the resulting force and bending angle for the continuum robot over time, while SMA2 and SMA3 are passive. Bottom shows the force over angle plot of a passive SMA1, when activating SMA2 and SMA3 simultaneously and equally using the same power inputs as shown in top left.

promising, is generally challenging when the SMA wires exhibit a nonlinear and hysteretic dependency between resistance and strain,[41] and thus will be investigated in future research work.

4. Conclusion and Outlook

This article has presented a novel systematic methodology to design SMA-driven continuum robots. Instead of developing a complete model incorporating the full hysteretic and nonlinear constitutive behavior of shape memory alloys, coupled with the nonlinear robot kinematics, the discussed approach enables for an accelerated and simplified design solely based on simple equations and graphical considerations.

First, the general 2D kinematic model of SMA-driven continuum robots is presented. This model is then expanded to a fully 3D moveable structure consisting of three SMA wires, being arranged equidistant to the core element with a 120° offset to each other. Validation of the presented models, based on specifically developed test rigs, shows errors of less than 6%. Furthermore, the measurements show a good approximation of the constant curvature kinematic assumption, with an error of 6% using only 4 spacer disks for a continuum robot with a backbone length of 100 mm. The results of the measurements with three-integrated SMA wires show a possible elongation of a single wire above $\varepsilon_T = 4\%$, when the other two wires are activated equally and simultaneously, as predicted with the model.

Future research investigations will focus on the validation of the structure 3D motion and workspace on the one hand, and on the extension to a fully integrated smart robot on the other hand. For the latter case, in particular, the self-sensing effect of SMA wires will be investigated measuring the electrical resistance of all three wires within different bending configurations. Using these findings will lead to further investigations, such as the possibility of reconstructing the robot configuration or detecting obstacles. Based on this, self-sensing motion control strategies will be developed and validated. Additional future investigations will focus on the thermal characterization of the SMA wires, and the optimization of the spacer disk's material as well as the electrical and mechanical connections to ensure a homogeneous phase transformation of the wires.

Conflict of Interest

The authors declare no conflict of interest.

Data Availability Statement

The data that support the findings of this study are available from the corresponding author upon reasonable request.

[1] P. Kumar Singh, C. M. Krishna, *Univers. J. Mech. Eng.* **2014**, *2*, 193.

[2] S. Kolachalama, S. Lakshmanan, *J. Rob.* **2020**, *2020*, Hindawi Limited.

[3] M. E. Pausley, S. Seelecke, in *Active and Passive Smart Structures and Integrated Systems 2008, SPIE*, March **2008**, p. 69280T, https://doi.org/10.1117/12.776212.

[4] G. Immega, K. Antonelli, in *IEEE Int. Conf. on Robotics and Automation*, Nagoya, Japan, May **1995**, pp. 3149–3154.

[5] J. M. M. Tur, W. Garthwaite, *J. Field Rob.* **2010**, *27*, 491.

[6] J. K. Hopkins, B. W. Spranklin, S. K. Gupta, *Bioinspiration Biomimetics* **2009**, *4*, 021001.

[7] M. A. Mandolino, Y. Goergen, P. Motzki, G. Rizzello, in *IEEE 17th Int. Conf. on Advanced Motion Control (AMC)*, Padova, Italy, February **2022**, pp. 6–11.

[8] V. Modes, J. Burgner-Kahrs, *IEEE Rob. Autom. Lett.* **2020**, *5*, 103.

[9] C. J. Nwafor, C. Girerd, G. J. Laurent, T. K. Morimoto, K. Rabenorosoa, *IEEE Trans. Rob.* **2023**, *39*, 2510.

[10] N. Simaan, K. Xu, W. Wei, A. Kapoor, P. Kazanzides, R. Taylor, P. Flint, *Int. J. Rob. Res.* **2009**, *28*, 1134.

[11] Y. Goergen, R. Chadda, R. Britz, D. Scholtes, N. Koev, P. Motzki, R. Werthschützky, M. Kupnik, S. Seelecke, in *ASME 2019 Conf. on Smart Materials, Adaptive Structures and Intelligent Systems, SMASIS 2019*, Louisville, KY, September **2019**, https://doi.org/10.1115/SMASIS2019-5610.

[12] G. Robinson, J. B. C. Davies, in *IEEE Int. Conf. on Robotics and Automation*, Detroit, MI, May **1999**, pp. 2849–2854.

[13] E. Amanov, T. D. Nguyen, J. Burgner-Kahrs, *Int. J. Rob. Res.* **2021**, *40*, 7.

[14] M. D. M. Kutzer, S. M. Segreti, C. Y. Brown, R. H. Taylor, S. C. Mears, M. Armand, in *Proc. IEEE Int. Conf. on Robotics and Automation*, Shanghai, China, May **2011**, pp. 2913–2920, https://doi.org/10.1109/ICRA.2011.5980285.

[15] R. Kang, Y. Guo, L. Chen, D. T. Branson, J. S. Dai, *IEEE/ASME Trans. Mechatron.* **2017**, *22*, 751.

[16] S. Zaidi, M. Maselli, C. Laschi, M. Cianchetti, *Curr. Rob. Rep.* **2021**, *2*, 355.

[17] C. Sun, L. Chen, J. Liu, J. S. Dai, R. Kang, *Proc. Inst. Mech. Eng. C J. Mech. Eng. Sci.* **2020**, *234*, 318.

[18] A. Isbister, N. Y. Bailey, I. Georgilas, *Front. Rob. AI* **2021**, *8*, 1.

[19] W. McMahan, B. A. Jones, I. D. Walker, in *2005 IEEE/RSJ Int. Conf. on Intelligent Robots and Systems*, IEEE, Edmonton, AB, Canada, August **2005**, pp. 2578–2585.

[20] F. Qi, F. Ju, D. Bai, Y. Wang, B. Chen, *Int. J. Med. Rob. Comput. Assisted Surg.* **2019**, *15*.

[21] P. Motzki, A. Bucht, K. Pagel, T. Mäder, S. Seelecke, in *Smart Materials - Eigenschaften Und Einsatzpotenziale*, 1st ed. (Ed: H. Böse), Vogel Communications Group, Würzburg **2023**, pp. 89–118.

[22] S. J. Furst, S. Seelecke, *J. Intell. Mater. Syst. Struct.* **2012**, *23*, 1233.

[23] H. Janocha, *Unkonventionelle Aktoren - Eine Einführung*, 2nd ed., Oldenburg Verlag, München **2013**.

[24] P. Motzki, *Advanced Design and Control Concepts for Actuators Based on Shape Memory Alloy Wires* **2018**.

[25] G. Rizzello, P. Motzki, in *Endorobotics: Design, R&D and Future Trends* (Ed: L. Manfredi), Academic Press, Cambridge, MA **2022**, pp. 117–163, https://doi.org/10.1016/B978-0-12-821750-4.00006-2.

[26] P. Motzki, S. Seelecke, *Encyclopedia of Smart Materials*, Elsevier, Amsterdam, Netherlands **2022**, pp. 254–266, https://doi.org/10.1016/B978-0-12-803581-8.11723-0.

[27] D. C. Lagoudas, *Shape Memory Alloys - Modeling and Engineering Applications*, Springer, New York, NY **2008**.

[28] N. Lewis, A. York, S. Seelecke, *Smart Mater. Struct.* **2013**, *22*, 094012.

[29] J. A. Shaw, S. Kyriakides, *J. Mech. Phys. Solids* **1995**, *43*, 1243.

[30] B. C. Chang, J. A. Shaw, M. A. Iadicola, *Continuum Mech. Thermodyn.* **2006**, *18*, 83.

[31] J. Van Humbeeck, *Mater. Sci. Eng. A* **1999**, *273–275*, 134.

[32] I. Dynalloy, *Technical Characteristics of Flexinol Actuator Wires*, Dynalloy, Inc., Irvine, CA.

[33] L. Fumagalli, F. Butera, A. Coda, *J. Mater. Eng. Perform.* **2009**, *18*, 691.

[34] L. Zhang, M. Xu, H. Yang, in *2017 IEEE Int. Conf. on Real-Time Computing and Robotics, RCAR 2017*, Okinawa, Japan, July **2018**, Vol. *2017-July*, pp. 74–78, https://doi.org/10.1109/RCAR.2017.8311839.

[35] R. Luo, T. Wang, Z. Shi, J. Tian, in *Proc. of 2017 IEEE 2nd Advanced Information Technology, Electronic and Automation Control Conf., IAEAC 2017*, Chongqing, China, March **2017**, pp. 157–161, https://doi.org/10.1109/IAEAC.2017.8053997.

[36] J. H. Crews, G. D. Buckner, *J. Intell. Mater. Syst. Struct.* **2012**, *23*, 545.

[37] C. Laschi, M. Cianchetti, B. Mazzolai, L. Margheri, M. Follador, P. Dario, *Adv. Rob.* **2012**, *26*, 709.

[38] S. J. Furst, J. H. Crews, S. Seelecke, *J. Intell. Mater. Syst. Struct.* **2013**, *24*, 1951.

[39] Y. Tian, M. Luan, X. Gao, W. Wang, L. Li, *Math. Probl. Eng.* **2016**, *2016*, 6984194.

[40] A. Gao, Y. Zou, Z. Wang, H. Liu, *J. Mech. Rob.* **2017**, *9*, 041019.

[41] J. Prechtl, S. Seelecke, P. Motzki, G. Rizzello, in *ASME 2020 Conf. on Smart Materials, Adaptive Structures and Intelligent Systems, SMASIS 2020*, September **2020**, https://doi.org/10.1115/SMASIS2020-2224.

[42] Y. Goergen, G. Rizzello, S. Seelecke, S. Motzki, in *ASME 2020 Conf. on Smart Materials, Adaptive Structures and Intelligent Systems, SMASIS 2020*, September **2020**, https://doi.org/10.1115/SMASIS2020-2213.

[43] B. Mazzolai, L. Margheri, M. Cianchetti, P. Dario, C. Laschi, *Bioinspiration Biomimetics* **2012**, *7*, 025005.

[44] X. An, Y. Cui, H. Sun, Q. Shao, H. Zhao, *IEEE Trans. Rob.* **2023**, *39*, 2325.

[45] M. R. Abdul Kadir, D. E. O. Dewi, M. N. Jamaludin, M. Nafea, M. S. Mohamed Ali, *Sens. Actuators, A Phys.* **2019**, *296*, 92.

[46] K. Ikuta, M. Tsukamoto, S. Hirose, in *IEEE Int. Conf. on Robotics and Automation (ICRA)*, Philadelphia, PA, April **1988**, pp. 427–430, https://doi.org/10.1109/robot.1988.12085.

[47] T. Mineta, T. Mitsui, Y. Watanabe, S. Kobayashi, Y. Haga, M. Esashi, *Sens. Actuators, A Phys.* **2001**, *88*, 112.

[48] W. Makishi, T. Matunaga, Y. Haga, M. Esashi, in *Proc. of the First IEEE/RAS-EMBS Int. Conf. on Biomedical Robotics and Biomechatronics, 2006, BioRob 2006*, Vol. *2006*, Pisa, Italy, February **2006**, pp. 217–219, https://doi.org/10.1109/BIOROB.2006.1639088.

[49] P. Rao, Q. Peyron, S. Lilge, J. Burgner-Kahrs, *Front. Rob. AI* **2021**, *7*, https://doi.org/10.3389/frobt.2020.630245.